

UNCLASSIFIED

Defense Technical Information Center  
Compilation Part Notice

ADP011809

TITLE: Thermal Sprayed Nanostructured Hard Coatings

DISTRIBUTION: Approved for public release, distribution unlimited

This paper is part of the following report:

TITLE: NATO Advanced Research Workshop on Nanostructured Films and Coatings. Series 3. High Technology - Volume 78

To order the complete compilation report, use: ADA399041

The component part is provided here to allow users access to individually authored sections of proceedings, annals, symposia, etc. However, the component should be considered within the context of the overall compilation report and not as a stand-alone technical report.

The following component part numbers comprise the compilation report:

ADP011800 thru ADP011832

UNCLASSIFIED

## THERMAL SPRAYED NANOSTRUCTURED HARD COATINGS

B.H. Kear and W.E. Mayo  
Rutgers, The State University of New Jersey  
Center for Nanomaterials Research  
607 Taylor Road  
Piscataway, NJ 08854-8065

### 1. Abstract

Hardcoatings of WC/12Co and  $\text{Al}_2\text{O}_3/13\text{TiO}_2$ , produced by High Velocity Oxy-Fuel (HVOF) and High Energy Plasma (HEP) spraying, have been investigated. In HVOF spraying, nanostructured WC/Co coatings experience more extensive decarburization than conventional coatings, whereas in HEP spraying, just the opposite effect occurs. This is explained in terms of the influence of temperature on the decarburization mechanism. In the  $\text{Al}_2\text{O}_3/13\text{TiO}_2$  case, HEP spraying generates a metastable coating, due to rapid quenching of the plasma melted particles on the substrate. The metastable phase has a defect spinel structure and a nanocrystalline grain size. When heated, it decomposes into an equilibrium two-phase structure, consisting of  $\alpha\text{-Al}_2\text{O}_3$  and  $\beta\text{-Al}_2\text{O}_3\cdot\text{TiO}_2$ . Both nanostructured cermets and ceramics have potential as wear-resistant coatings.

### 2. Introduction

Materials with fine-scale structures have long been recognized to exhibit remarkable and technologically attractive properties. Over the past decade [1-3], interest has been growing in a new class of materials that are composed of ultra-fine grains or particles. A feature of such *nanostructured* materials is the high fraction of atoms that reside at grain boundaries or interfaces in the materials. Although much of today's R&D activity is focused on the synthesis and processing of nanostructured bulk materials [3,4], there is a growing interest in the fabrication of nanostructured coatings.

This paper presents a progress report on work being conducted on thermal spraying of nanostructured hardcoatings at Rutgers' Center for Nanomaterials Research, in collaboration with several industrial partners. Our work in this area has been focussed primarily on developing wear-resistant coatings of WC/12Co and  $\text{Al}_2\text{O}_3/13\text{TiO}_2$ .

### 3. Experimental

*Feed powders* of conventional and nanostructured WC/12Co were obtained from Surface Engineering (2400 grade) and Nanodyne (Nanocarb®), respectively. These powders have strikingly different characteristics, which are a consequence of different production methods.

Conventional WC/Co powder is produced by mechanical mixing of WC and Co particles in a fluid medium, spray drying to form solid agglomerates, and heat treatment to consolidate the agglomerated particles. Nanostructured WC/Co powder is produced by spray drying an aqueous solution mixture of salts of the constituent elements to develop a homogeneous precursor powder, followed by fluid bed thermochemical conversion (pyrolysis, reduction and carburization) of that powder to form the desired nano-WC/Co end-product powder [5,6]. During the cool-down cycle in the reactor, the high surface area powder is passivated with oxygen-rich species. Without this precautionary measure, the powder is susceptible to spontaneous combustion when exposed to air.

The as-produced conventional powder consists of solid agglomerates, which are screened to a relatively narrow size distribution, typically within the range 15-40  $\mu\text{m}$ . Within each particle the carbide grain size is from 2-5  $\mu\text{m}$ . In contrast, the as-produced nanostructured powder has a porous, spherical shell morphology, and particle size of 5-30  $\mu\text{m}$ . The individual WC grains residing within each nanocomposite particle are about 30-50 nm.

*Thermal spraying* was carried out at A&A Company Inc., using both HVOF and HEP guns. Plasma spraying was performed with a Metco 3M gun, using both Ar/10% He and  $\text{N}_2/12\% \text{H}_2$  as feed gases. The much longer particle residence time in the hot zone of the  $\text{N}_2/\text{H}_2$ -plasma, due to release of recombination energy downstream in the plasma jet, heats up the particles to much higher temperatures. Therefore, the trend in thermal spraying, represented by HVOF, Ar/He-plasma and  $\text{N}_2/\text{H}_2$ -plasma, reflects a sharp increase in the mean particle temperature achieved during spraying.

## 4. Results and Discussion

### 4.1 WC/12Co COATINGS

#### 4.1.1 HVOF Deposition

Coating tests were performed with an HVOF gun, using both conventional and nanostructured powder feeds of the same nominal composition, WC/12Co; actual compositions are given in Table I. Metallographic examination of cross-sections of the two types of coatings revealed some important differences in their microstructures.

In the nano-coating case, a typical microstructure consisted of alternating bands of speckled and clear material, and inter-band porosity, Figure 1. Under high resolution in the SEM, a speckled region of the microstructure was revealed to be a highly porous aggregate of WC and Co particles, Figure 2(a), reminiscent of the original particle structure. Moreover, it appeared that many of the WC nanoparticles were experiencing

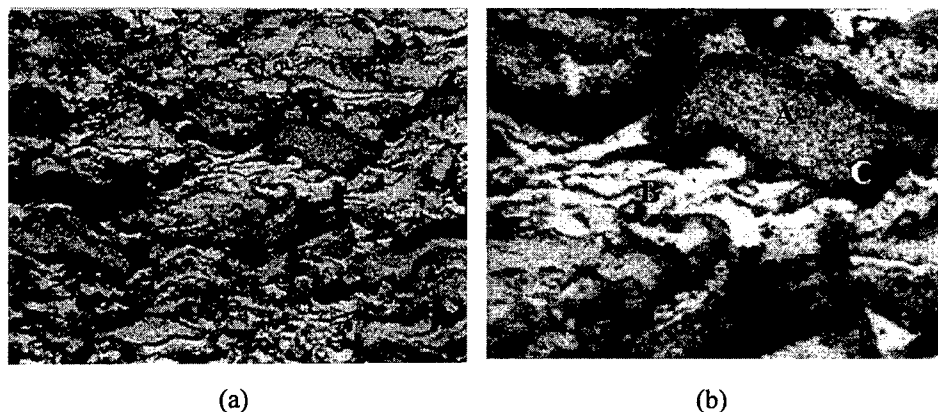


*Figure 1.* Optical micrographs (etched and re-polished) of HVOF-sprayed WC/12Co nano-coating; (a) low magnification (400x) micrograph showing "banded" structure of coating, and (b) same area at higher magnification (1000x) showing speckled band (A), clear band (B), and inter-band porosity (C).

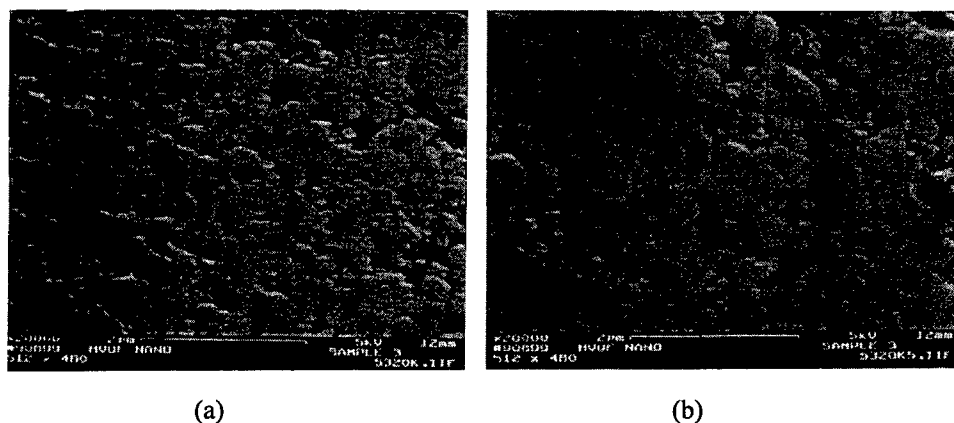


*Figure 2.* SEM micrographs of the different regions in Figure 1, showing (a) extensive micro-porosity in a speckled band (A), and (b) the absence of such porosity in a clear band (B). Both bands show the presence of a fine distribution of WC particles, but they appear to be coarser in the pore-free band of the microstructure.

coarsening by a particle rearrangement and coalescence mechanism. Evidence for this mechanism is indicated in Figure 2(a), where clusters of WC nanoparticles appear to be coalescing to form larger particles, apparently assisted by the presence of liquid Co. In contrast, a clear region of the microstructure, Figure 2(b), was composed of a pore-free, sintered mass of WC particles in a Co matrix phase, although the amount of Co phase was larger than expected. As will be shown later, this is explicable on the grounds that

these regions must have been exposed to high temperatures during spraying, thus causing some dissolution of the WC particles in the liquid Co to form more liquid phase. Another feature is the larger average particle size in Figure 2(b) relative to Figure 2(a), which is consistent with a higher temperature of exposure of the latter during thermal spraying. A surprising finding is the faceting of many of the WC particles, down to the smallest particle size observable, which is indicative of good wetting between the WC particles and the liquid Co phase. Such an effect is commonly observed in the near-equilibrium conditions encountered in liquid phase sintering of bulk materials [7].

Table I

		Material	Composition (wt.pct)				
			W	Co	Total C	Free C	O/N (ppm)
Surface Eng. powder feed (WC/15Co)	{	Starting powder	79.87	14.94	5.19	0.04	1670/480
		HVOF coating	79.98	15.1	4.85	0.07	5730/460
		Plasma coating	98.17	0.55	1.28	0.05	2260/280
Nanodyne powder feed (WC/12Co)	{	Starting powder	82.63	12	5.37	0.04	1000/200
		HVOF coating	84.44	11.66	3.9	0.09	1770/140
		Plasma coating	92.6	4.76	2.65	0.12	2380/70

These observations are interpreted to be evidence for non-uniform melting of the original shell-like particles during spraying. As indicated in Figure 3, only the liquid phase sintered part of a heated particle would be expected to yield a dense structure when it impacts the chilled substrate. In contrast, the heated, but not necessarily melted part of that same particle should retain at least some, if not all, of its original micro-porosity. In agreement with this model, the hardness in the clear regions was ~1050 VHN (1 kg load), whereas that in the speckled regions was ~650 VHN (1 kg load)—the latter reflecting ‘softening’ of the region by virtue of the presence of a fine distribution of micro-pores. In other words, despite a relatively uniform distribution of WC particles, the presence of micro-porosity substantially reduces the measured hardness of the coating.

If the temperature of any region of a heated particle exceeds the melting temperature of the pseudo-binary eutectic in the WC-Co system [8], rapid dissolution of the WC nanoparticles in the liquid Co is to be expected, assisted by the high surface area of contact between the two phases. Thus, the amount of liquid Co, and its enrichment in W and C, should both increase progressively with degree of superheat above the eutectic temperature. Such an effect would explain the variations in WC particle size and distribution in the clear regions of the microstructure. Moreover, enrichment of the liquid Co in W and C should generate a high population density of strong tungsten/carbon clusters in the liquid phase, making it highly susceptible to

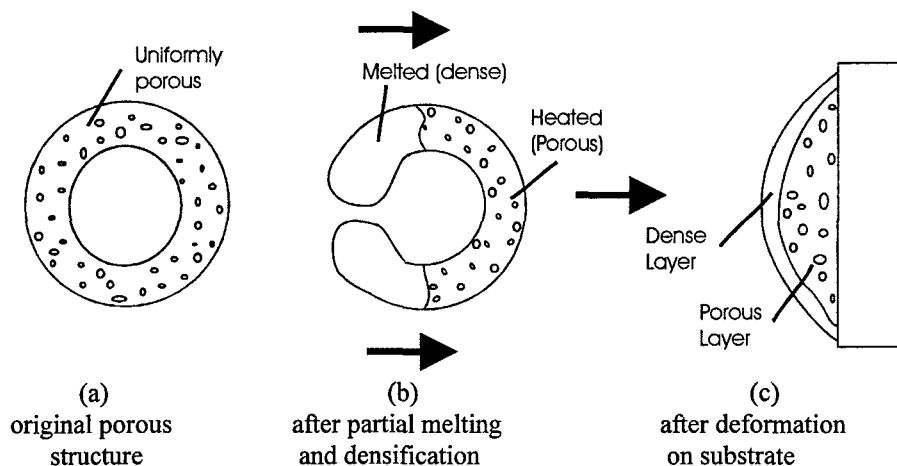


Figure 3. Schematic representation of the formation of a "banded" coating structure when a partially melted and densified nano-WC/Co particle impacts on the substrate surface.

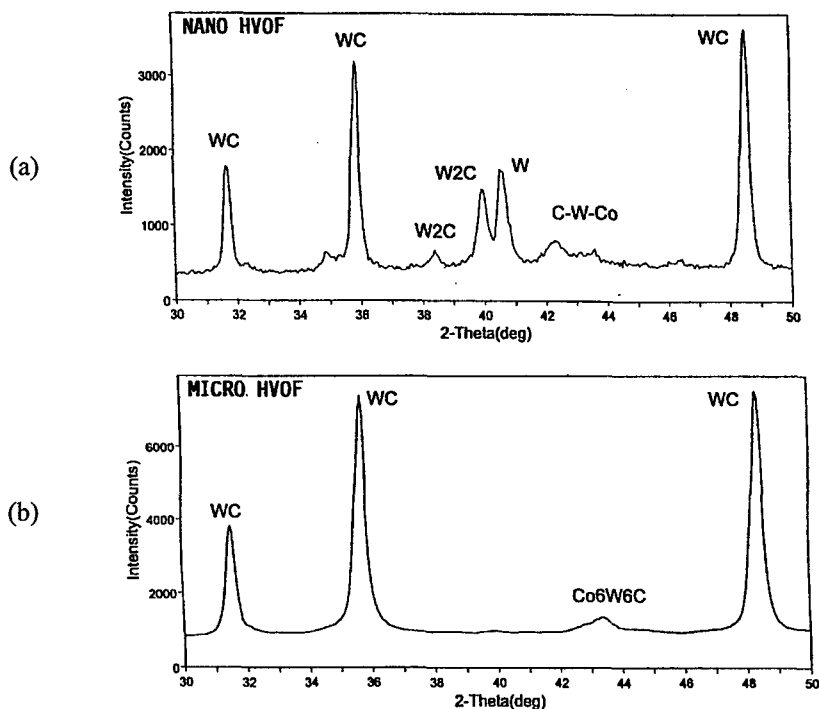
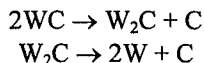


Figure 4. X-ray diffraction patterns of HVOF-deposited WC/12Co coatings, showing evidence for more decarburization in the nano-coating sample (a), relative to the micro-coating sample (b).

amorphization during subsequent solidification. Since the Co-rich liquid experiences splat-quenching on the chilled substrate, it seems inevitable that an amorphous Co-rich matrix phase will be developed, as in fact has been reported in the literature [9,10]. On the other hand, if the quenching rate is not high enough, then crystallization of mixed-metal carbide nanophases is to be expected. Evidence for  $\eta$ -carbide formation on an ultra-fine scale has been found in X-ray diffraction patterns of some of the coatings.

X-ray diffraction patterns of the two types of coatings showed that decarburization was more pronounced in the nano-coating material than in the micro-coating material, Figure 4. The most prominent feature in the diffraction pattern of the nano-coating material is the evidence for  $W_2C$  and W formation, which accounts for about 30% of the total carbide content in the material. This behavior is believed to be a consequence of two effects. First, loss of WC phase can occur by high temperature reaction with oxygen in the HVOF environment, leading to the formation of  $W_2C$  and even W. This includes impurity oxygen in the feed gases, on the surfaces of the passivated nanoparticles, and by mixing of ambient air with the combustion flame. Second, if the temperature is high enough, then the WC particles can undergo thermal decomposition, according to the following reactions:



The instability of WC phase at high temperatures is well known [11], but what is not known is how this is affected by the presence of liquid Co. It seems likely that dissolution of WC in liquid Co must play a role, but the details are unclear at this time.

In the nano-coating case, it is believed that the high surface area of the nano-WC/Co particles makes decarburization by reaction with impurity oxygen the dominant mechanism, thus accounting for the observed higher degree of decarburization relative to that of the micro-coating case, Figure 4. On the other hand, under the conditions encountered in plasma spraying, where particle temperatures are much higher, the dominant decarburization mechanism is thermally-induced decomposition of the WC phase, as will be shown later.

Because of the importance of the microstructural features discussed above, coating samples from several thermal spray companies were examined. Without exception, all HVOF-derived nano-coatings showed a heterogeneous microstructure, similar to that of Figure 1. However, different samples showed varying degrees of inter-band porosity and relative volume fractions of speckled (micro-porous) and clear (dense) regions, which is taken to be an indication of the importance of controlling thermal spray parameters to produce nano-coatings with reproducible microstructures, properties and performance.

The observations on the HVOF-deposited micro-coatings were similar to that reported in the literature [12]. The most significant feature was the relatively uniform distribution of coarse WC particles in the Co matrix phase. An important difference was the absence of significant dissolution of WC particles in the liquid Co, because of the low surface area of contact between the two phases. Another factor was the relatively low enrichment of the Co phase in W and C in the starting powder, relative to that of the nano-powder, which is enriched in W and C by virtue of the chemical route used in its production.

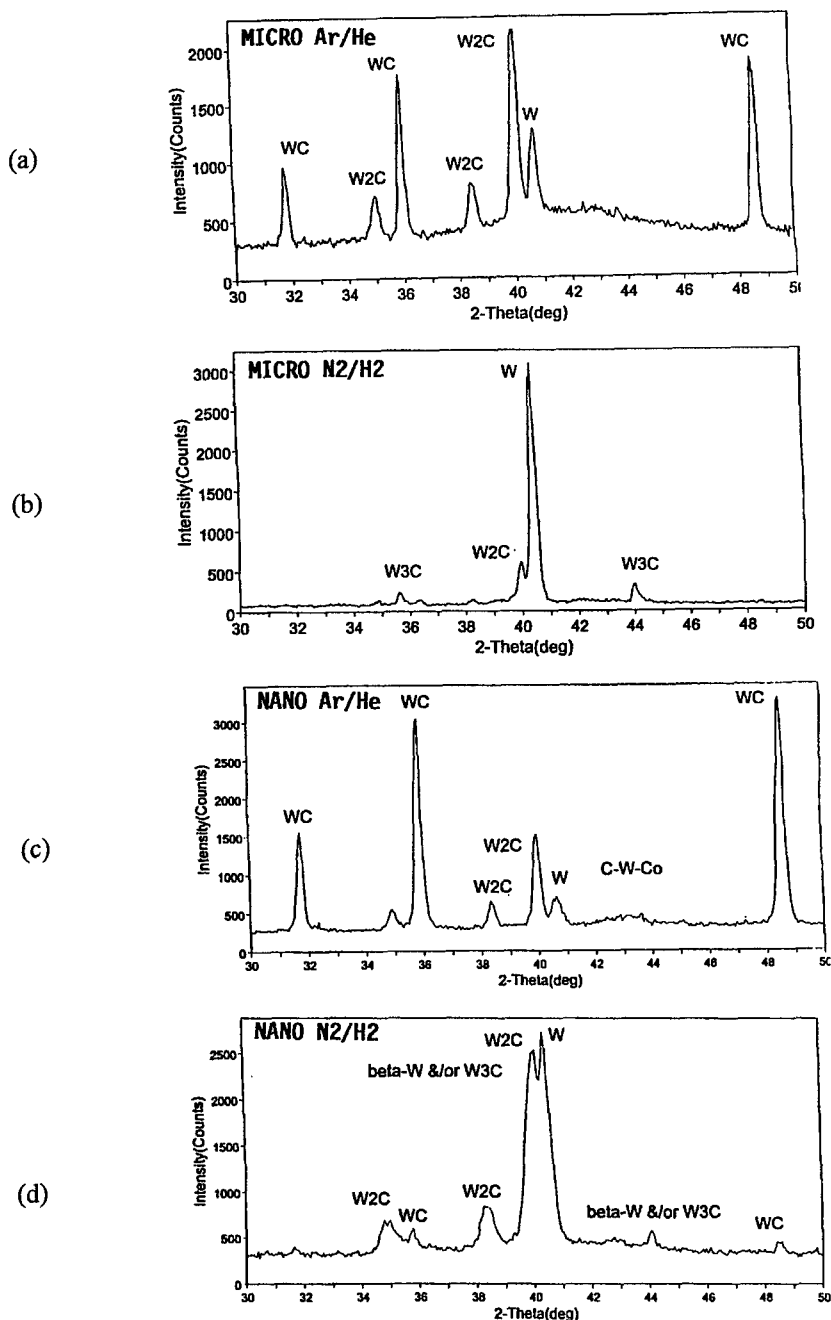


Figure 5. X-ray diffraction patterns of HEP-deposited WC/12Co coatings, showing evidence for more extensive decarburization in the micro-coating samples (a) and (b), relative to the nano-coating samples (c) and (d).



#### 4.1.2 HEP deposition

Coating tests were performed with an HEP gun, using Ar/10% He and N<sub>2</sub>/12% H<sub>2</sub> feed gases.

X-ray diffraction patterns showed evidence for extensive decarburization in the HEP-deposited coatings, but the effect was more pronounced in micro-coatings than in nano-coatings, Figure 5, which was the opposite of that found for HVOF-deposited coatings, Figure 4. The sequence of phase changes was strikingly different in the two cases. In the micro-coating case, decarburization involved the formation of W<sub>2</sub>C and W at the expense of WC. However, the major phase was W<sub>2</sub>C in the Ar/He plasma coating, and W in the N<sub>2</sub>/H<sub>2</sub> plasma coating. In contrast, in the nano-coating case, decarburization to form W<sub>2</sub>C and W was not as pronounced.

Chemical analysis of HVOF and N<sub>2</sub>/H<sub>2</sub> plasma coatings confirmed the trend in decarburization indicated by the X-ray analysis. Moreover, there was clear evidence for a major loss of Co, which was quite remarkable in the micro-coating case. As shown in Table I, the amount of Co decreases from 15 wt.% in the starting powder to 0.55 wt.% in the N<sub>2</sub>/H<sub>2</sub>-plasma coating, and there is a corresponding decrease in carbon content from 5.19 wt.% to 1.28 wt.%. Similar losses of Co and C occurred in the nano-coating case, but not as much as that in the micro-coating case.

The microstructure of a N<sub>2</sub>/H<sub>2</sub>-plasma coating was quite different from that of an HVOF coating, irrespective of the type of powder feed used, i.e. nano- versus micro-powder. This was most clearly seen in a comparison of etched samples of the nano-coating material. The HVOF coating showed a uniform distribution of WC particles, Figure 6(a), whereas there was little or no evidence for such particles in the N<sub>2</sub>/H<sub>2</sub>-plasma coating, Figure 6(b). A similar difference in microstructure was seen in an HVOF overlay coating on a N<sub>2</sub>/H<sub>2</sub>-plasma coating, Figure 6(c). This difference in etching behavior is consistent with Figure 5, which shows that the major phases are W and W<sub>2</sub>C, with only a small amount of residual WC phase due to extensive decarburization. Similar observations were made for the micro-coating material, except that banding of the microstructure was more pronounced. The microstructures of the corresponding Ar/He -plasma coatings more closely resembled the HVOF coatings than the N<sub>2</sub>/H<sub>2</sub>-plasma coatings, particularly in the nano-coating case, again consistent with the X-ray data.

Hardness measurements on both nano- and micro-coatings showed consistently higher values for HVOF coatings relative to N<sub>2</sub>/H<sub>2</sub>-plasma coatings, reflecting the more extensive decarburization experienced in plasma spraying. Moreover, there was little difference in hardness between transverse and in-plane sections of the microstructure, Table II, despite the presence of microstructural banding. In a few cases, the dependence of hardness on coating thickness was examined. A surprising finding was the reproducible decrease in hardness with coating thickness for both micro-coating and nano-coating samples, with a HVOF coating consistently displaying higher hardness than a N<sub>2</sub>/H<sub>2</sub>-plasma coating. It should be noted that the hardness values obtained at low loads were consistently higher than that at high loads, due to the influence of porosity in the coatings. Nevertheless, the trends in hardness observed were the same whatever the magnitude of load applied.

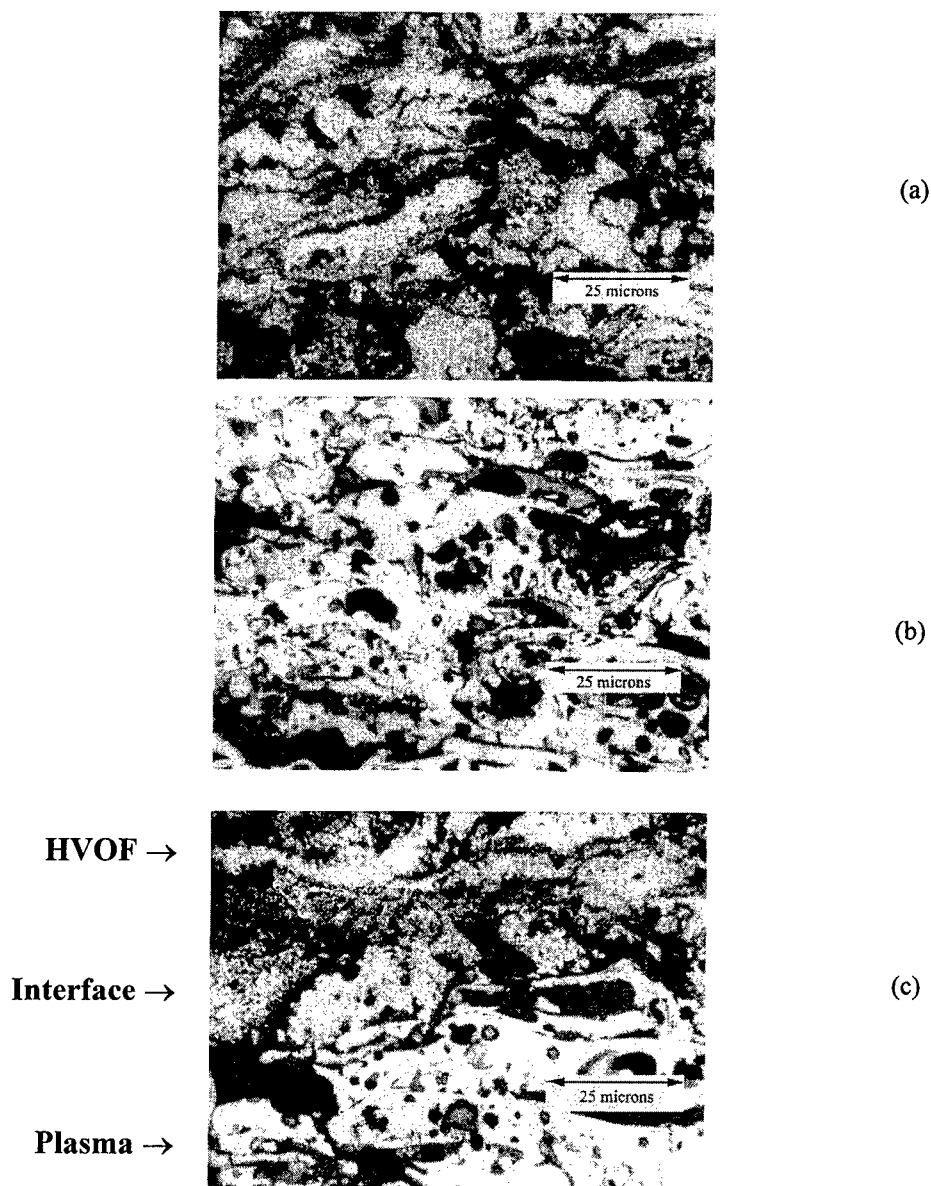


*Figure 6.* Optical micrographs of WC/12Co nano-coating samples, comparing microstructures (etched condition) of (a) HVOF coating, (b)  $N_2/H_2$ -plasma coating, and (c) HVOF overlay coating on  $N_2/H_2$ -plasma coating. Note uniform distribution (speckled appearance) of fine WC particles in (a), and the absence of WC particles in (b), due to extensive decarburization in the  $N_2/H_2$ -plasma coating.

Table II

Coating	Transverse section		In-plane section	
	VHN <sub>100</sub>	VHN <sub>1000</sub>	VHN <sub>100</sub>	VHN <sub>1000</sub>
HVOF	1233	744	1156	644
Plasma	937	414	871	474
HVOF +	1187	666	---	---
Plasma	946	414	---	---

The variations in hardness with coating thickness in nano- and micro-coating samples are not understood. It is conceivable that the build-up of internal stresses during incremental coating deposition is a contributing factor. This will be checked by further experiments.

#### 4.1.3 Decarburization mechanism

Taken together, these observations provide strong evidence for the decarburization model discussed above. A key factor is the much higher average particle temperature achieved during plasma spraying, relative to HVOF spraying, which causes more extensive decarburization. A surprising result is the almost complete decarburization of the micro-coating using a  $N_2/H_2$ -plasma, as well as the gross loss of Co. Evidently, in this case, particle temperatures are so high that vaporization of Co and C occur to an unusual degree, even during the very short residence times in the hot zone of the plasma. It is proposed that the reduced susceptibility of the nano-coating to these compositional changes reflects the lowering of the vapor pressure of the liquid Co because of its enrichment in W and C. The mechanism of C gasification needs further investigation, but it may be enhanced by reactions with the ionized gas species in the plasma.

#### 4.1.4 Coating thickness effect

There have been indications that much thicker coatings can be produced using nanostructured powder feed than conventional powder feed. This is a useful result, since in many applications there are requirements for thick coatings that are beyond today's capabilities. A feature of the microstructure that needs more attention is the presence of micro-porosity in the thermal sprayed nano-coating material. Since these micro-porous regions are not as hard and stiff as the adjacent melted and quenched regions, this raises interesting questions concerning the potential for relaxation of internal stresses in the softer regions during coating deposition. In other words, the build up of internal stresses during incremental deposition may be lessened, so that the coating may be less prone to cracking and/or de-bonding at the coating/substrate interface. This topic is currently under investigation

## 4.2 $Al_2O_3/13TiO_2$ COATINGS

Agglomerated powder feed of  $Al_2O_3/13TiO_2$ , (Metco 130, particle size  $-53 \mu m + 15 \mu m$ ) was obtained from Sulzer Metco. An X-ray diffraction pattern of this powder

showed that it was composed of a micron-scale mixture of  $\alpha$ - $\text{Al}_2\text{O}_3$  (corundum) and  $\text{TiO}_2$  (anatase) grains.

Plasma spraying was carried out at A&A Company Inc. using a Metco 3M gun. The powder was fed into a high energy  $\text{N}_2/10\%\text{H}_2$  plasma, with a protective argon shroud, and sprayed into cold water and onto a chilled substrate, located at about 23 cm. from the gun nozzle. The resulting powders, splats and coatings were characterized by X-ray diffraction, using  $\text{Cu}_{K\alpha}$  radiation (40 kV, 30 mA), and JADE (version 3.1) for phase identification. Vickers hardness measurements were performed on polished sections using a Leco micro-hardness tester.

#### 4.2.1 Effect of cooling rate

During the short residence time in the plasma jet, the feed particles were completely melted and homogenized. When the liquid droplets were water quenched, they solidified in one of two microstructural forms. Particles experiencing moderate cooling rates ( $\sim 10^4$  °K/sec) displayed a well-defined dendritic microstructure, and exhibited some phase separation. However, particles experiencing somewhat higher cooling rates developed a cellular-dendritic microstructure. Both of these microstructures are shown in Figure 7. When the cooling rate was exceptionally high,  $\sim 10^6$  °K/sec, as in splat-quenching on a metal chill plate, the microstructure was featureless. In other words, it appears that segregation-less (plane-front) solidification occurs only under the highest cooling rates characteristic of splat-quenching [13].

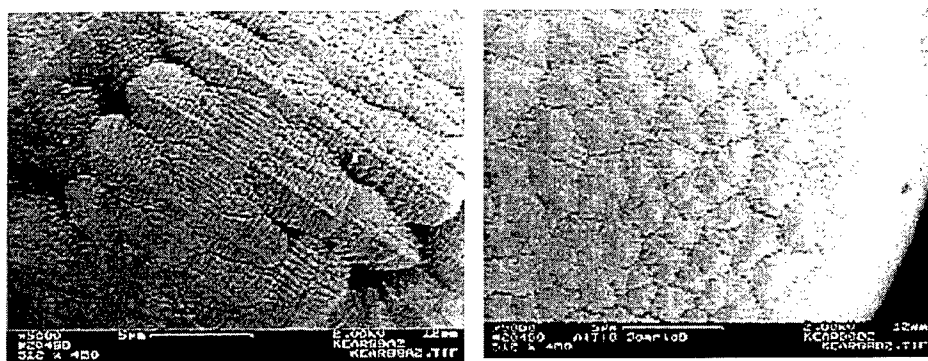


Figure 7. SEM micrographs of plasma-melted and water-quenched particles of  $\text{Al}_2\text{O}_3/\text{TiO}_2$ , showing dendritic (left) and cellular-dendritic (right) microstructures, depending on cooling rate.

An X-ray diffraction pattern of the water-quenched powder, Figure 8, shows that the dendritic structure is composed of an amorphous component,  $\alpha$ - $\text{Al}_2\text{O}_3$ , and metastable  $\text{Al}_2\text{O}_3 \bullet \text{TiO}_2$ , which we call  $\chi$ -phase. Our calculations indicate that the powder has approximately 50% amorphous content, 40%  $\chi$ -phase, and 10%  $\alpha$ - $\text{Al}_2\text{O}_3$ . The grain size of  $\alpha$ - $\text{Al}_2\text{O}_3$  is approximately 60 nm, whereas that of the  $\chi$ -phase is about 24 nm. In contrast, the corresponding X-ray diffraction pattern of splat-quenched

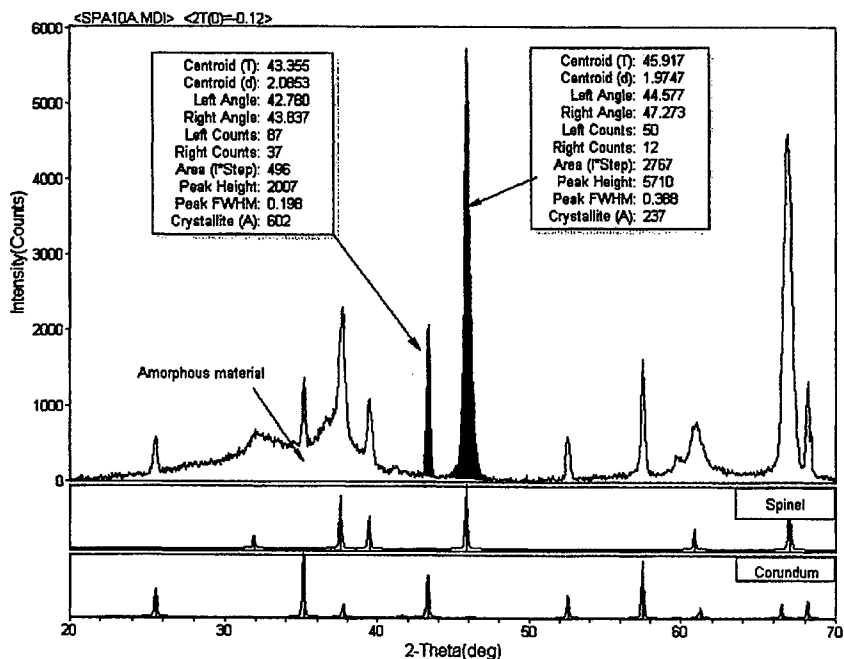


Figure 8. X-ray diffraction pattern of  $\text{Al}_2\text{O}_3/\text{TiO}_2$  powder, after plasma melting and water quenching. Shown for comparison are the reference diffraction patterns for the spinel and corundum ( $\alpha\text{-Al}_2\text{O}_3$ ) structures.

powder, Figure 9, shows evidence for a strong amorphous component plus  $\chi$ -phase (28 nm grain size), but no  $\alpha\text{-Al}_2\text{O}_3$ . The absence of  $\alpha\text{-Al}_2\text{O}_3$  phase is believed to be a consequence of the much higher average cooling rate experienced by splat-quenched material, relative to water-quenched material.

X-ray diffraction patterns similar to that of  $\chi$ -phase have been reported in the literature. In particular, Zhou and Snyder [14] have given a detailed analysis of the diffraction patterns of chemically synthesized  $\eta\text{-Al}_2\text{O}_3$  and  $\gamma\text{-Al}_2\text{O}_3$  powders, Figure 10. Both phases have a cubic structure - spinel with  $\text{Fd}3\text{m}$  space group. In this structure, the oxygen ions form a cubic close-packed sub-lattice, and the aluminum ions partially occupy both octahedral and tetrahedral sites. The broad peaks indicate a high degree of structural disorder, so that the material is more properly described as having a defect spinel structure. An exception is the sharp (222) reflection, which is due to scattering from ordered domains of the oxygen sub-lattice.

In the present case, Figure 9, the relative intensities of the (400) and (440) reflections are the opposite of that displayed by the  $\eta$  and  $\gamma$  phases. Computer simulations indicate that there is a preference for octahedral coordination of the cations, and that there is random occupancy of Ti on the Al lattice sites. It may be concluded, therefore, that  $\chi$ -phase is a metastable solid solution of  $\text{Al}_2\text{O}_3$  and  $\text{TiO}_2$ . There are

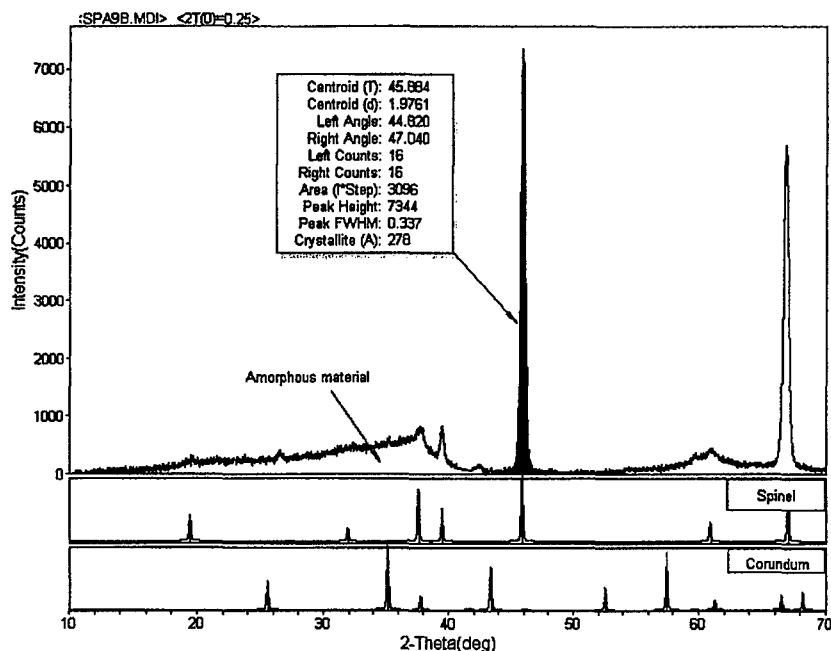


Figure 9. X-ray diffraction pattern of  $\text{Al}_2\text{O}_3/\text{TiO}_2$  powder, after plasma melting and splat quenching on a copper chill plate. Shown for comparison are the reference diffraction patterns for the spinel and corundum ( $\alpha\text{-Al}_2\text{O}_3$ ) structures.

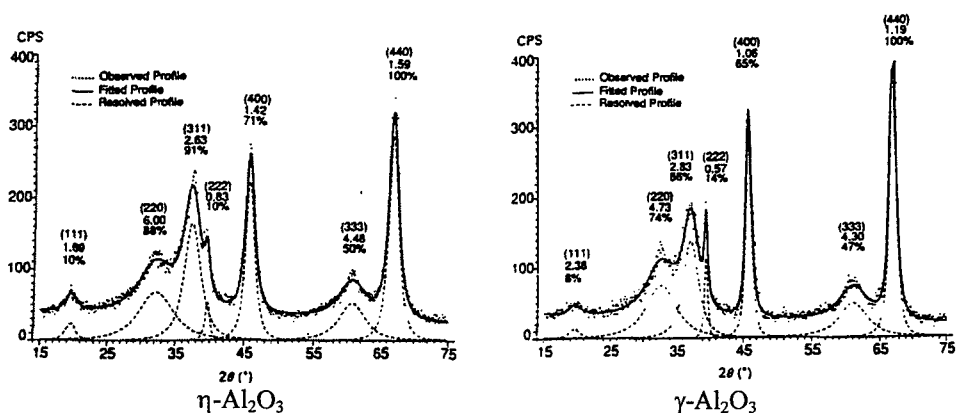


Figure 10. X-ray diffraction patterns of chemically-synthesized  $\eta\text{-Al}_2\text{O}_3$  and  $\gamma\text{-Al}_2\text{O}_3$  powders, after Zhou and Snyder [14].

several features in the diffraction pattern that indicate a strongly disordered structure, which is far from equilibrium. First, note the presence of an amorphous phase, as indicated by the "hump" in the diffraction pattern at  $35^\circ$ . Also, the diffraction peaks are strong only for the spinel peaks at approximately  $46^\circ$  and  $66.5^\circ$ . All the other peaks for this phase have very low intensity.

An X-ray diffraction pattern of a typical plasma-sprayed coating showed similar features to that of the splat-quenched powder. This is to be expected, since a coating is formed by the superposition of splat-quenched particles. On the other hand, thick coatings produced by multiple passes showed some indications of  $\alpha\text{-Al}_2\text{O}_3$  formation, which probably reflects heating of the substrate, and hence lowering of the average quench rate.

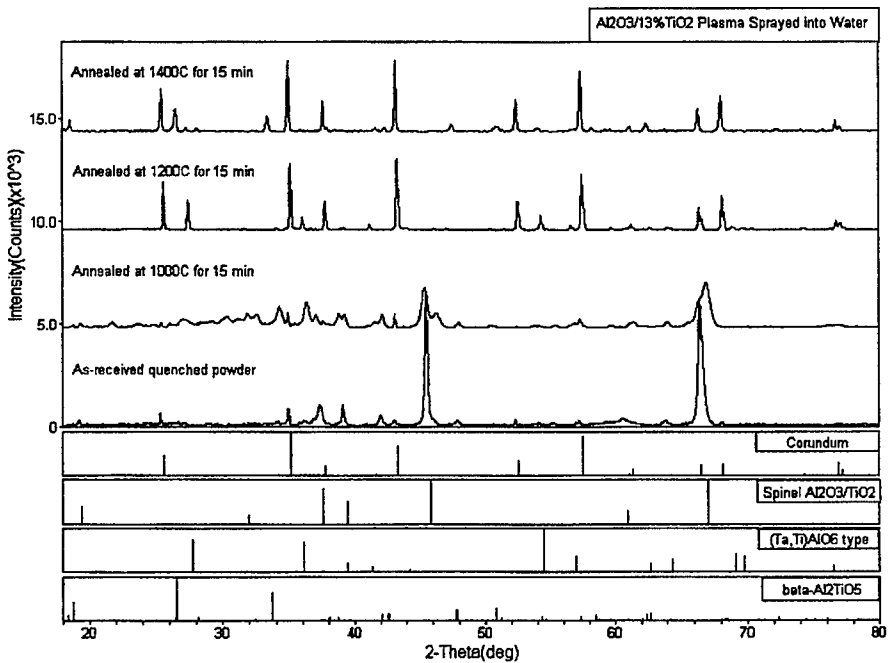


Figure 11. X-ray diffraction patterns of water-quenched and heat treated  $\text{Al}_2\text{O}_3/\text{TiO}_2$  powder, showing decomposition reactions with increasing temperature.

#### 4.2.2 Effect of heat treatment

When water-quenched powder is heated at temperatures below  $1200^\circ\text{C}$ , a series of intermediate phases are formed, Table III. At  $1000^\circ\text{C}$ , the first such intermediate phase to appear has an unknown structure, with no known structural analogue. At  $1200^\circ\text{C}$ , a tetragonal phase appears, which is similar to the  $(\text{Ta,Ti})\text{Al}_2\text{O}_6$  crystal structure described in Powder Diffraction File #32-0028 [15]. This phase is also metastable, and further decomposes at  $1400^\circ\text{C}$  into the equilibrium two-phase structure, consisting of

Table III  
Summary of Heat Treatment Data  
Water-quenched powder

Annealing Temperature	Qualitative Composition (Main Phases)		Approximate Quantitative Composition	Color
RT	x-phase	$\alpha$ -Alumina	10:1	blue
800°C	x-phase	$\alpha$ -Alumina	4:1	blue
1000°C	x-phase	$\alpha$ -Alumina unidentified phase(s)	2:1:1	blue-grey
1200°C	$\alpha$ -Alumina	y-phase	1:1	yellow-white
1400°C	$\alpha$ -Alumina	$\beta$ -Aluminum Titanate y-phase	10:10:1	white

x-phase: cubic,  $a_0=7.94\text{\AA}$ ;  $\text{Al}_2\text{O}_3 \cdot \text{TiO}_2$

cell dimensions close to those of  $\gamma$ -alumina (defect spinel structure)

y-phase: tetragonal  $a_0=4.59$ ,  $c_0=2.96$ ;  $\text{Al}_2\text{O}_3 \cdot \text{TiO}_2$

cell dimensions close to that of  $\text{AlTiTaO}_6$ .

Table IV  
Summary of Heat Treatment Data  
Splat-quenched coating

Annealing Temperature	Qualitative Composition (Main Phases)		Approximate Quantitative Composition	Hardness (kg/mm <sup>2</sup> , 1 kg load)
RT	x-phase			700
800°C	x'-phase*			720
1000°C	$\alpha$ -Alumina	x-phase or $\gamma$ -Alumina unidentified phase(s)	5:1:1	850
1200°C	$\alpha$ -Alumina	$\text{Ti}_3\text{O}_5$	10:1	940
1400°C	$\alpha$ -Alumina	$\beta$ -Aluminum Titanate	1:1	990

x-phase: cubic,  $a_0=7.94\text{\AA}$ ;  $\text{Al}_2\text{O}_3 \cdot \text{TiO}_2$

cell dimensions close to those of  $\gamma$ -alumina (defect spinel structure)

\*x'-phase: cell dimensions close to x-phase

$\beta$ -phase: orthorhombic  $a_0 = 9.439$ ,  $b_0 = 9.647$ ,  $c_0 = 3.592$



approximately 1:1 mixture of  $\alpha$ - $\text{Al}_2\text{O}_3$  and  $\beta$ - $\text{Al}_2\text{O}_3 \cdot \text{TiO}_2$  (orthorhombic structure, PDF #41-0258). Thus, the final structure consists of primary  $\alpha$ - $\text{Al}_2\text{O}_3$  (micrometer scale), and secondary  $\alpha$ - $\text{Al}_2\text{O}_3$  that co-precipitates with the  $\beta$ - $\text{Al}_2\text{O}_3 \cdot \text{TiO}_2$ . Figure 11 illustrates these phase transitions via their respective X-ray diffraction patterns.

When splat-quenched material (powder or coating) is heated, thermal decomposition of the original  $\chi$ -phase follows a somewhat different path, Table IV. The most notable change is the appearance of  $\alpha$ - $\text{Al}_2\text{O}_3$  at 1000 °C as a major phase. Again, however, the equilibrium two-phase structure is established at 1400 °C. These phase transitions with increasing temperature are accompanied by a progressive increase in hardness, as indicated in Table IV. It is significant that the final structure at 1400 °C has a Vickers hardness of 990 kg./mm<sup>2</sup>, which represents about a 40% increase over that of the as-sprayed coating. An important feature is the absence of micron-scale primary  $\alpha$ - $\text{Al}_2\text{O}_3$  in the final nanocomposite material, which is a reflection of the structural uniformity of the original splat-quenched material.

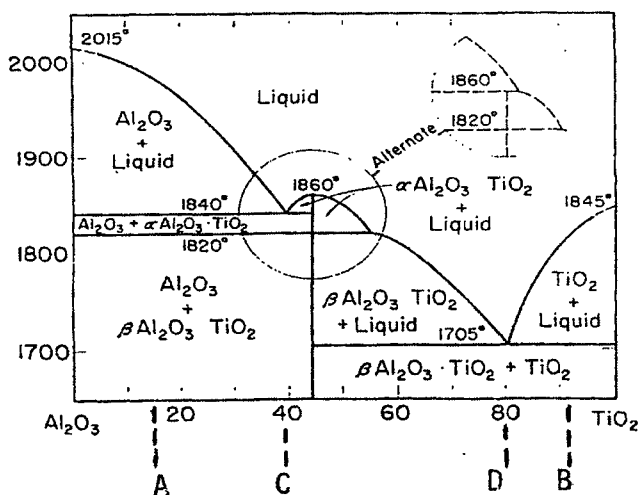


Figure 12. Phase diagram for the  $\text{Al}_2\text{O}_3$ - $\text{TiO}_2$  system, after Lang, Fillmore and Maxwell [15].

#### 4.2.3 Compositional effect

The location of the  $\text{Al}_2\text{O}_3/13\text{TiO}_2$  composition on the equilibrium phase diagram is indicated in Figure 12. The presence of the nanocrystalline  $\alpha$ - $\text{Al}_2\text{O}_3$  phase in the water-quenched powder, Figure 8, can be interpreted as a consequence of significant undercooling of the melt prior to nucleation of primary  $\alpha$ - $\text{Al}_2\text{O}_3$  grains followed by dendritic growth of the principal  $\chi$ - $\text{Al}_2\text{O}_3/\text{TiO}_2$  phase. This being the case, the volume fraction of the much harder  $\alpha$ - $\text{Al}_2\text{O}_3$  phase may be increased by shifting the composition towards the  $\text{Al}_2\text{O}_3$ -rich side of the phase diagram. It is difficult to predict the composition requirement to realize say a 50:50 mixture of the two phases, because

of the modification of the phase diagram under supercooling conditions. However, it seems that a starting composition of about  $\text{Al}_2\text{O}_3/7\text{TiO}_2$  might serve the purpose. Experiments are underway to check this concept.

## 5. Acknowledgements

Support from the Office of Naval Research (contract numbers N00014-97-1-0249; N00014-97-1-0844; and N00014-98-3-0005) is gratefully acknowledged.

## 6. References

1. Gleiter, H. (1989) Nanocrystalline materials, *Progress in Materials Science*, **33**, (4) 223.
2. Kear, B.H. and Strutt, P.R. (1995) Nanostructures, the next generation of high performance bulk materials and coatings, *KONA Powder and Particle*, **13**, pp. 45-55.
3. Siegel, R.W. (1993) Synthesis and properties of nanophase materials, *Mat. Sci. Eng. A: Structural Materials: Properties, Microstructure and Processing*, **2**, pp. 189-197.
4. Sadangi, R.K., McCandlish, L.E., Kear, B.H. and Seegopaul, P. (1998) Grain growth inhibition in liquid phase sintered nanophase WC/Co alloys, in Oakes, J.J. and Reinshagen, J.H. (eds.) *Proc. 1998 Int. Conf. on Powder Metallurgy and Particulate Materials*, MPIF, pp. 1-51.
5. McCandlish, L.E., Kear, B.H. and Bhatia, J., Spray conversion process for production of nanophase WC-Co powders, US Patent No. 5,352,269.
6. McCandlish, L.E., Kear, B.H. and Kim, B.K. (1990) Chemical processing of nanophase WC-Co composite powders, *Mats. Sci. & Tech.*, **6**, pp. 953-957.
7. German, R.M. (1985) *Liquid Phase Sintering*, Plenum Press, New York.
8. Schwarzkopf, P. and Keiffer, R. (1960) *Cemented Carbides*, Macmillan, London.
9. McCandlish, L.E., Kear, B.H., Kim, B.K. and Wu, L. (1990) Low pressure plasma sprayed coatings of nanophase WC-Co, in Yazici, R.M. (ed.), *Protective Coatings: Processing and Characterization*, The Minerals, Metals and Materials Society, pp. 113-143.
10. Li, C.J., Ohmori, A. and Harada, Y. (1996) Formation of an amorphous phase in thermally sprayed WC-Co coatings, *Journal of Thermal Spray Technology* **5**, (1), pp. 69-73.
11. Binary phase diagram of W-C, (1992) ASM Handbook, **3**, p. 2.115.
12. Sampath, S. and Herman, H. (1992) *Thermal Spray Technology*, ASM, Materials Park, OH.
13. Cohen, M., Kear, B.H. and Mehrabian, R. (1980) Rapid solidification processing--an outlook, *Proc. Second Int. Conf. on Rapid Solidification Processing*, Reston, VA, p. 1.
14. Zhou, R.-S. and Snyder, R.L. (1991) Structures and transformation mechanisms of the  $\eta$ ,  $\gamma$  and  $\theta$  transition aluminas, *Acta Cryst.* **B47**, pp. 617-630.
15. Lang, S.M., Fillmore, C.L. and Maxwell, L.H. (1952) *J. Research Natnl. Bur. Standards*, **48**, (4) p. 301; RP 2316.